https://doi.org/10.1007/s11467-022-1244-4

RESEARCH ARTICLE

Reversible doping polarity and ultrahigh carrier density in two-dimensional van der Waals ferroelectric heterostructures

Yanyan Li[1], Mingjun Yang[1], Yanan Lu[1], Dan Cao[2], Xiaoshuang Chen[3], Haibo Shu[1,†]

[1] College of Optical and Electronic Technology, China Jiliang University, Hangzhou 310018, China

[2] College of Science, China Jiliang University, Hangzhou 310018, China

[3] National Laboratory for Infrared Physics, Shanghai Institute of Technical Physics, Chinese Academy of Science, Shanghai 200083, China

Corresponding author. E-mail: †shuhaibo@cjlu.edu.cn

Received May 22, 2022; accepted September 5, 2022

Supporting Information

S1. Interfacial configurations and stabilities of 2D TMD/In_2X_3 VSHs

2D TMD/In_2X_3 VSHs were created by vertically stacking a 2×2 TMD monolayer on $\sqrt{3} \times \sqrt{3}$ α-In_2X_3 nanosheets for the minimization of lattice mismatch. According to the polar-axis orientation (P_{down} and P_{up}), these VSHs can be divided into TMD/In_2X_3(↓) and TMD/In_2X_3(↑), respectively. The most stable interfacial configuration of each TMD/In_2X_3 VSH was determined by the energy comparison among various potential interfacial configurations. As shown in Fig. S5a and b, six interfacial configurations have been considered. Taking $MoTe_2$/1L-In_2Se_3 VSHs as an example, the energy comparison shows that A-configuration is the most stable one for $MoTe_2$/1L-In_2Se_3(↑) VSH and C-configuration is the most stable one for $MoTe_2$/1L-In_2Se_3(↓) VSH. The similar results have been found in other TMD/In_2X_3 VSHs. Based on the optimal interface configurations, the optimized lattice parameters and energetic data of $MoTe_2$/In_2Se_3 and $MoSe_2$/In_2S_3 VSHs are listed in Table S1 and Table S2, respectively.

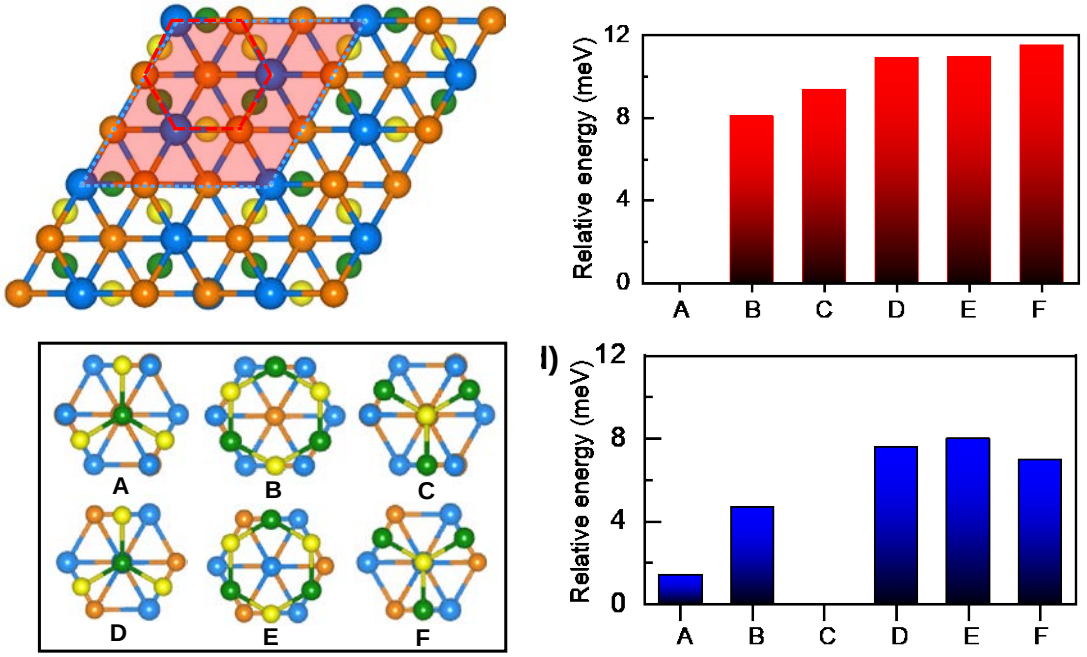

Fig. S1 Interfacial configurations and energetics of 2D TMD/In_2X_3 (X = S, Se) VSHs. **(a)** Top view of atomic structures of $MoTe_2/In_2Se_3$ and $MoSe_2/In_2S_3$ VSHs. The shadow region indicates the unit cell range of these VSHs. **(b)** Six potential interfacial configurations (A-F) of TMD/In_2X_3 VSHs. **(c)** Relative energies of $MoTe_2$/1L-In_2Se_3(↑) VSH with the configurations A-F. The total energy of the configuration A is used as a reference. **(d)** Relative energies of $MoTe_2$/1L-In_2Se_3(↓) VSH with the configurations A-F. The total energy of the configuration C is used as a reference.

Table S1 Optimized in-plane lattice constant (a), interface distance (d), interfacial binding energies (γ_{int}), interface dipole moments (μ), and electrostatic potential difference ($\Delta\Phi$) of $MoTe_2/In_2Se_3$ VSHs. The thickness range of In_2Se_3 layer is considered from 1L to 4L. $MoTe_2/In_2Se_3$(↑) and $MoTe_2/In_2Se_3$(↓) denote the VHSs in P_{up} and P_{down} state, respectively.

Heterostructures	$MoTe_2/In_2Se_3$(↑)				$MoTe_2/In_2Se_3$(↓)			
	1L	2L	3L	4L	1L	2L	3L	4L
a (Å)	6.740	6.662	6.661	6.661	6.651	6.661	6.660	6.660
d (Å)	3.39	3.35	3.32	3.32	3.33	3.29	3.26	3.25
γ_{int} (J/m^2)	-0.19	-0.20	-0.25	-0.24	-0.20	-0.21	-0.26	-0.28
μ (Deby)	1.68	3.60	4.08	4.11	1.49	2.16	2.26	2.30
$\Delta\Phi$ (eV)	1.50	3.16	3.92	3.98	1.25	1.81	1.92	1.94

Table S2 Optimized in-plane lattice constant (a), interface distance (d), interfacial binding energies (γ_{int}), interface dipole moments (μ), and electrostatic potential difference ($\Delta\Phi$) of $MoSe_2/In_2S_3$ VSHs. The thickness range of In_2S_3 layer is considered from 1L to 4L. $MoSe_2/In_2S_3$(↑) and $MoSe_2/In_2S_3$(↓) denote the VHSs in P_{up} and P_{down} state, respectively.

Heterostructures	$MoSe_2/In_2S_3$(↑)				$MoSe_2/In_2S_3$(↓)			
	1L	2L	3L	4L	1L	2L	3L	4L
a (Å)	6.42	6.41	6.41	6.41	6.42	6.41	6.41	6.41
d (Å)	2.77	2.74	2.74	2.74	2.48	2.40	2.35	2.32
γ_{int} (J/m^2)	-0.15	-0.18	-0.19	-0.20	-0.28	-0.45	-0.66	-0.83
μ (Deby)	0.83	1.21	1.52	1.52	0.81	0.72	0.58	0.56
$\Delta\Phi$ (eV)	3.28	4.58	5.09	4.88	2.37	2.15	2.25	2.20

S2. Ferroelectric polarization effect on electrostatic potentials of 2D α-In_2X_3 nanosheets

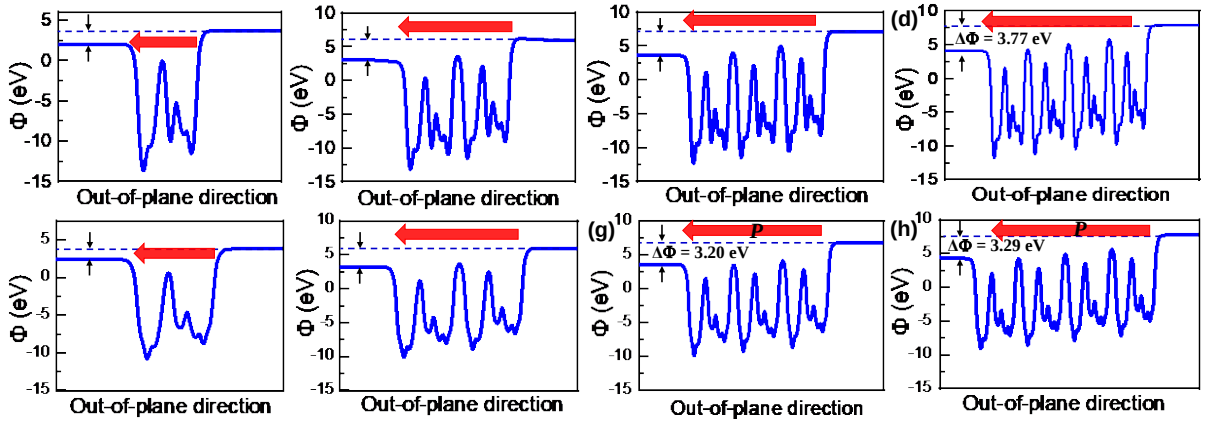

Fig. S2 Average electrostatic potential distribution (Φ) of 2D α-In_2X_3 (X = S, Se) ferroelectrics with the thickness range from 1L to 4L. **(a-d)** The Φ of 2D α-In_2S_3 with the thickness range from 1L to 4L. **(e-h)** The Φ of 2D α-In_2Se_3 with the thickness range from 1L to 4L. The ΔΦ denote the electrostatic potential difference between two surface terminations of the 2D α-In_2X_3 ferroelectrics. The arrows indicate the polarization direction. It can be seen that all considered 2D α-In_2X_3 nanosheets indicate asymmetric electrostatic potential distribution along the out-of-plane direction (or polarization direction), suggesting the existence of ferroelectric polarization field.

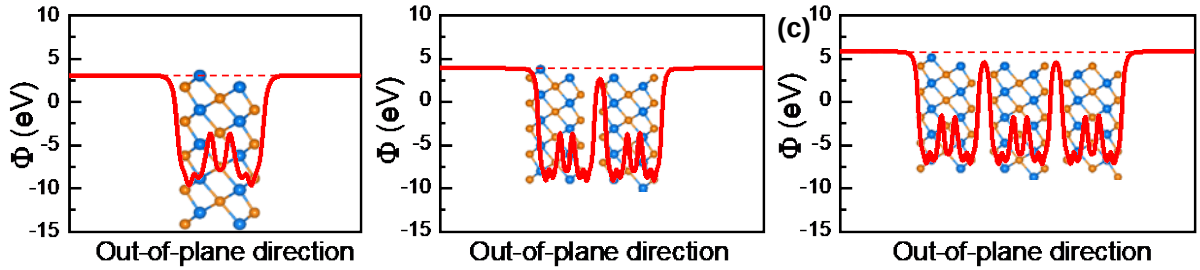

Fig. S3 Average electrostatic potential distribution (Φ) of 2D β-In_2Se_3 nanosheets with the layer thickness of **(a)** 1L, **(b)** 2L, and **(c)** 3L. The electrostatic potentials of all the β-In_2Se_3 nanosheets indicate symmetric distribution along the out-of-plane (or *z*-axis) direction. Irrespective of the layer thickness, the electrostatic potentials of β-In_2Se_3 nanosheets are symmetric along the out-of-plane direction. Therefore, there is no spontaneous polarization in these β-In_2Se_3 nanosheets.

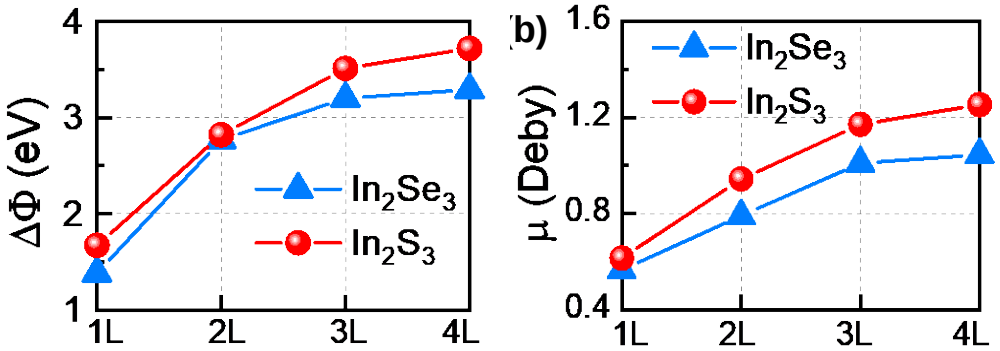

Fig. S4 Thickness-dependent **(a)** ΔΦ and **(b)** dipole moment (μ) in 2D α-In_2X_3 (X = S, Se) ferroelectrics. These data were obtained by the HSE06 functional. It can be seen that both the ΔΦ and μ values of these α-In_2X_3 ferroelectrics can be gradually saturated with the increase of layer thickness.

S3. Band structures of 2D In_2X_3 nanosheets

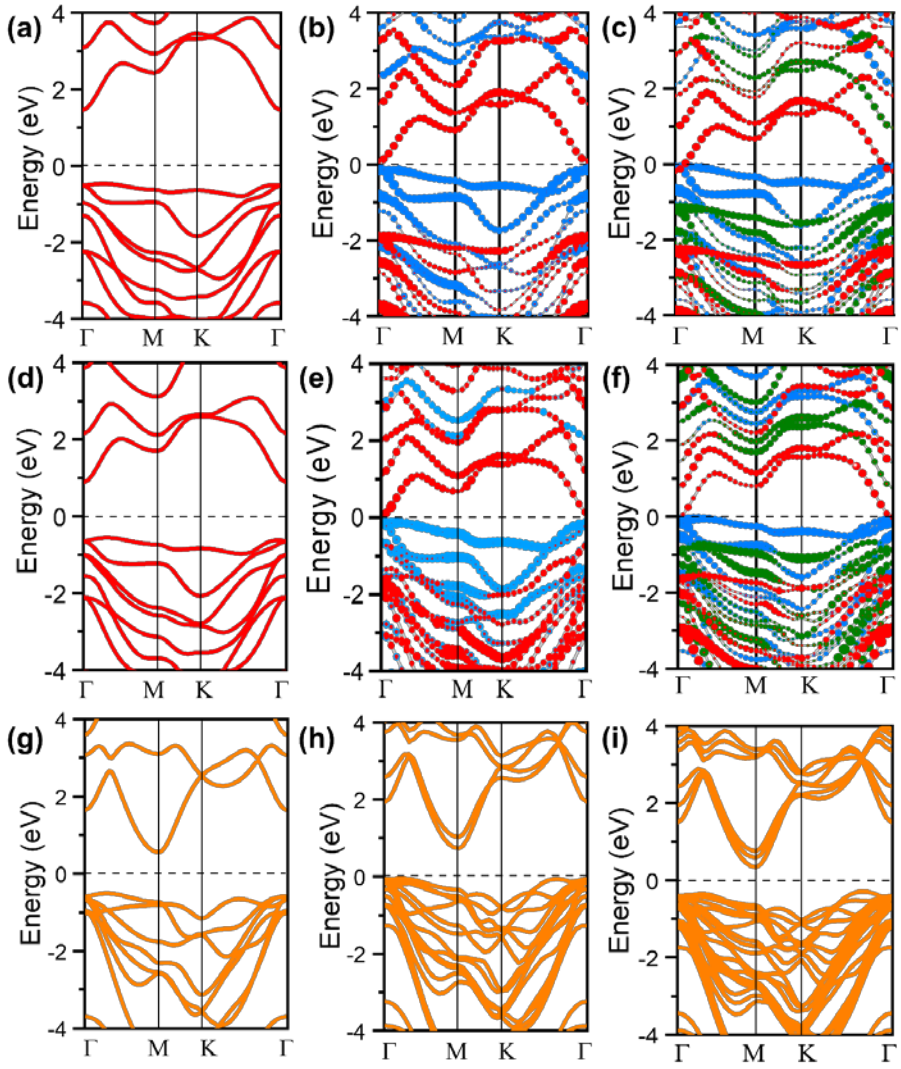

Fig. S5 Band structures of 2D In_2X_3 (X = S, Se) nanosheets calculated by the HSE06 functional. **(a-c)** Projected band structures of α-In_2S_3 ferroelectrics with the thickness range from 1L to 3L. **(d-f)** Projected band structures of α-In_2Se_3 ferroelectrics with the thickness range from 1L to 3L. The blue, green, and red bands are contributed by the top-layer, middle-layer, and bottom-layer In_2X_3 along the polarization direction, respectively. **(g-i)** Band structures of 2D β-In_2Se_3 nanosheets with the thickness range from 1L to 3L. The dash lines denote the position of Fermi level. There is no layer-by-layer band shift in band structures of β-In_2Se_3 nanosheets due to the lack of ferroelectric polarization field.

S4. Thickness effect on projected band structures of $MoTe_2/In_2Se_3$ VSHs

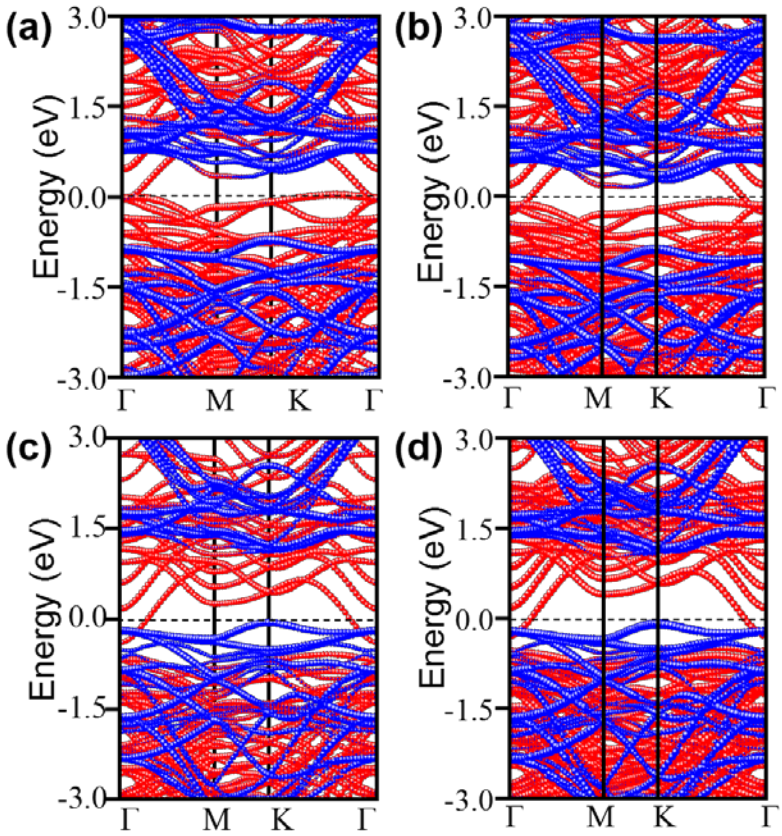

Fig. S6 Projected band structures of $MoTe_2/In_2Se_3$ VSHs with different In_2Se_3 layer thicknesses in P_{up} and P_{down} states calculated by the PBE functional. **(a, b)** Projected band structures of $MoTe_2/In_2Se_3(\uparrow)$ VSHs with (a) 3L-In_2Se_3 and (b) 4L-In_2Se_3. **(c, d)** Projected band structures of $MoTe_2/In_2Se_3(\downarrow)$ VSHs with (c) 3L-In_2Se_3 and (d) 4L-In_2Se_3. The red and blue bands denote the contribution from the In_2Se_3 and $MoTe_2$ layers, respectively. The black dash lines denote the position of Fermi level. When the thickness of In_2Se_3 layer arrives at 3L, the further increase of In_2Se_3 layer will bring few changes of band-edge electronic states in the VSHs. More specifically, the $MoTe_2/In_2Se_3(\uparrow)$ VSHs exhibit metallic characteristic and their band-edge electronic states around the Fermi level are contributed by the In_2Se_3 layer. This originates from the formation of self-doped p-n junctions in the In_2Se_3 layer of the VSHs. The band alignment characteristic of $MoTe_2/In_2Se_3$ VSHs is not sensitive to the thickness change of In_2Se_3 layer from 3L to 4L. For the $MoTe_2/In_2Se_3(\downarrow)$ VSHs, the CBM state contributed by the In_2Se_3 layer is lower than the Fermi level and the VBM state contributed by the $MoTe_2$ layer is higher than the Fermi level, consequently resulting in the formation of vdW p-n junctions in the VSHs. Moreover, the self-doping characteristic of $MoTe_2/In_2Se_3(\downarrow)$ VSHs is also not sensitive to the thickness change of In_2Se_3 layer.

S5. Band alignments of $MoSe_2/In_2S_3$ VSHs

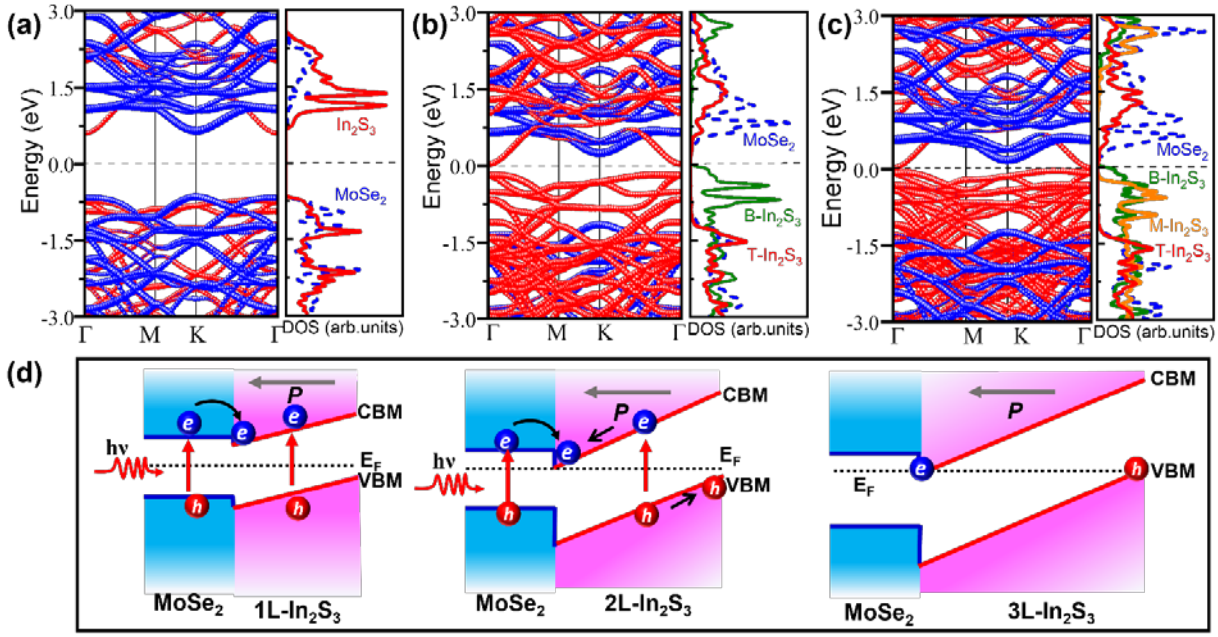

Fig. S7 Band alignments of 2D $MoSe_2/In_2S_3(\uparrow)$ VSHs with the thickness range of In_2S_3 layer from 1L to 3L. **(a-c)** Projected band structure and DOS of VSH with (a) 1L-In_2S_3, (b) 2L-In_2S_3, and (c) 3L-In_2S_3. The red and blue bands denote the contribution from In_2S_3 and $MoSe_2$ layers, respectively. The horizontal dash lines denote the position of Fermi level. T-In_2S_3, M-In_2S, and B-In_2S_3 represent the top-layer, middle-layer, and bottom-layer In_2S_3 in the VSHs, respectively. **(d)** Schematic of band alignments of $MoSe_2/In_2S_3(\uparrow)$ VSHs. The black and gray arrows denote the carrier transport direction and polarization direction, respectively.

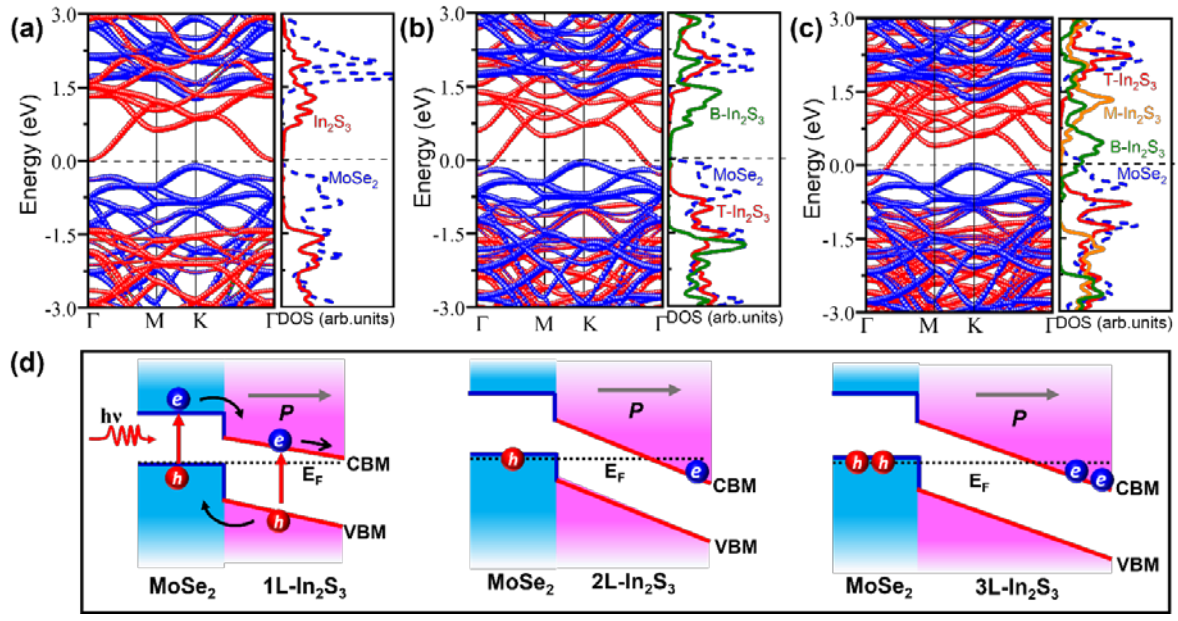

Fig. S8 Band alignments of 2D $MoSe_2/In_2S_3(\downarrow)$ VSHs with the thickness range of In_2Se_3 layer from 1L to 3L. **(a-c)** Projected band structure and DOS of VSH with (a) 1L-In_2S_3, (b) 2L-In_2S_3, and (c) 3L-In_2S_3. The red and blue bands represent the contribution of In_2S_3 and $MoSe_2$ layers, respectively. The horizontal dash lines denote the position of Fermi level. T-In_2S_3, M-In_2S_3, and B-In_2S_3 represent the top-layer, middle-layer, and bottom-layer In_2S_3 in the VSHs, respectively. **(d)** Schematic of band alignments of $MoSe_2/In_2S_3(\downarrow)$ VSHs. The arrows indicate the polarization direction.

S6. FE phase transition driven evolution of band-edge states in $MoTe_2/In_2Se_3$ VSH

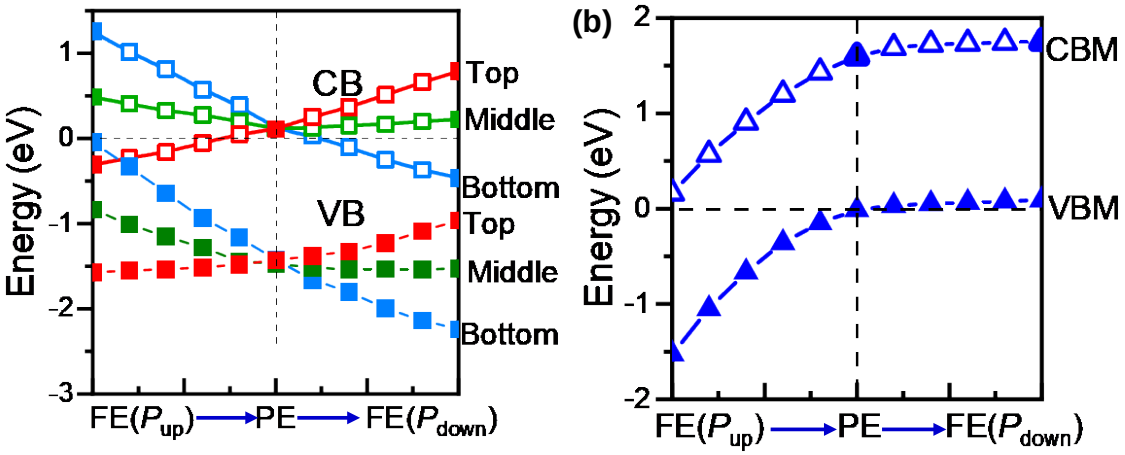

Fig. S9 Ferroelectric phase transition driven band-edge-position evolution of **(a)** In_2Se_3 layer and **(b)** $MoTe_2$ layer in $MoTe_2$/3L-In_2Se_3 VSH. The filled and unfilled points denote the conduction-band and valence -band data, respectively. The red, green, and blue points represent the data of T-In_2Se_3, M-In_2Se_3, and B-In_2Se_3, respectively.